International Journal of Biological Macromolecules 381 (2026) 154004

Contents lists available at ScienceDirect

International Journal of Biological Macromolecules

journal homepage: www.elsevier.com/locate/ijbiomac

Calcium modulates activity and stability in a novel halotolerant *endo*-mannanase

Marco Orlando [a,1], Mattia Salvadori [a], Panagiotis F. Sarris [b], Marco Mangiagalli [a], Marina Lotti [a,*]

[a] Department of Biotechnology and Biosciences, University of Milano-Bicocca, Milano, Italy
[b] Department of Biology, University of Crete, Heraklion, 70013, Greece

ARTICLE INFO

Keywords:
Glycosidase
GH26 family
Halophilic microorganism
Mannan degradation
Glutamicibacter

ABSTRACT

β-Mannanases are involved in the hydrolysis of mannan, a major component of hemicellulose. The genome of *Glutamicibacter halophytocola* sp., an endophytic bacterium isolated from *Crithmum maritimum*, a halophilic plant from the Island of Crete, encodes a putatively secreted β-mannanase (Gh_GH26) belonging to glycoside hydrolase 26 family (GH26). This sequence occupies a poorly explored region of the GH26 sequence space. Gh_GH26 consists of three domains, including a C-terminal carbohydrate-binding module 23 (CBM23), which is uncommon among GH26s and has a peculiar amino acidic composition at the −3/−4 substrate subsites. Gh_GH26 displays halophilic behavior, retaining activity up to 2.5 M NaCl, and exhibits *endo*-mannanase activity.

Functional analyses combined with structural predictions suggest that Gh_GH26 coordinates Ca^{2+} ions through a single binding site located within the CBM23 domain. The residues involved in Ca^{2+} binding are conserved in the CBMs of other characterized GH26s, despite their low similarity with Gh_GH26. Site-directed mutagenesis shows that Ca^{2+} ions contribute to both enzyme activity and stability. These results suggest that Ca^{2+} may play an evolutionary conserved activation role, modulating CBM flexibility and its orientation relative to the catalytic domain.

Overall, this work expands our understanding of the functional and structural diversity of the GH26 family, highlighting its potential for application in the degradation of mannan-containing biomass under saline conditions.

1. Introduction

β-Mannan-containing polysaccharides are abundant components in the hemicellulose of roots and seeds of various plant species [1,2], and of the cell walls of fungi and diatoms [3,4]. This diverse group of glycans includes both homopolymer mannan- and glucomannan heteropolymers. Mannan consists of a linear backbone of β-1,4-linked D-mannose monomers [5], whereas glucomannan features a backbone of β-1,4-linked D-mannose and D-glucose alternating in different proportions [6]. Both polysaccharides can be decorated with α-1,6-galactosyl branches on D-mannose residues and/or modified by acetylation [2,7]. To degrade and remodel these polysaccharides, nature has evolved sophisticated enzymatic machineries composed of carbohydrate-active enzymes (CAZymes) [8]. Among them, glycoside hydrolases (GHs) initiate the extracellular hydrolysis by cleaving long polysaccharide chains into oligosaccharides. Oligosaccharides are transported into the cell, where intracellular GHs complete their breakdown into monomers. As multiple synergistic enzymes and transport proteins are required, the genes encoding these systems are frequently organized into the same operon or clustered in polysaccharide utilization loci [3,9]. The first step in β-mannans degradation is catalysed by β-1,4-mannanase (EC 3.2.1.78), also known as β-mannanase. This enzyme acts through an *endo*-action mechanism that cleaves β-1,4-mannosidic bonds, producing mannooligosaccharides (MOS) of varying lengths, which may retain α-1,6-galactosyl branches [10]. β-1,4-mannanases are classified within GH families GH5, GH26, GH113, and GH134. Subsequently, MOS are hydrolyzed into mannose by exo-1,4-β-mannobiohydrolases (EC 3.2.1.100, GH families 1, 2, and 5, [8]), while residual α-1,6-galactosyl branches are removed by *exo*-α-1,6-galactosidase (EC 3.2.1.22, GH families 27 and 36). β-mannanase and exo-1,4-β-mannobiohydrolases have attracted significant interest for biotechnological applications. These enzymes can be used to treat

* Corresponding author at: Department of Biotechnology and Biosciences, University of Milano-Bicocca, Piazza della Scienza 2, 20126, Milano, Italy.
E-mail address: marina.lotti@unimib.it (M. Lotti).
[1] Present address: Laboratory for Environmental and Life Sciences, University of Nova Gorica, Slovenia.

https://doi.org/10.1016/j.ijbiomac.2026.154004
Received 13 April 2026; Received in revised form 9 July 2026; Accepted 7 August 2026
Available online 12 August 2026

β-mannan-rich biomasses to reduce their viscosity and increase their solubility in water. This enzymatic treatment improves the release of monosaccharides such as D-mannose, D-glucose, and D-galactose, which are used as energy sources for microbial cell factories [11]. Moreover, β-mannanases are employed in food processing for the preparation of MOS formulations, which are valued as prebiotics or postbiotics [12,13].

Microorganisms from extreme environments, such as high-salinity habitats, are valuable sources of robust enzymes adapted to harsh conditions [14]. Halotolerant and halophilic enzymes maintain their structure and catalytic activity under high salt concentrations despite lower water solvation [15,16]. Plant-growth-promoting bacteria that colonize the tissues of salt-tolerant plants can exploit host-derived polysaccharides, including β-mannan-containing polysaccharides [17,18], for their metabolism. Consequently, the CAZymes they secrete, including β-mannanases, are expected to be active at high salt concentrations.

Crithmum maritimum is an annual pioneer plant species commonly found along the Mediterranean seacoast. Exposed to periodic seawater submersion and high-salinity sandy soil, *C. maritimum* has evolved salt tolerance mechanisms, including salt secretion and accumulation in its leaves [19]. Recent studies have shown that *Glutamicibacter halophytocola* sp. is a halotolerant strain capable of growing up to 10% salt concentration. It inhabits the apoplast of *C. maritimum* roots, where it acts as a plant-growth-promoting bacterium, enhancing the host's salt-tolerance response [20,21].

In this study, we report on the functional and structural characterization of an evolutionary novel GH26 from *G. halophytocola* CrR6. This halotolerant enzyme acts as an *endo*-β-mannanase and its activity and stability are modulated by Ca^{2+} coordination.

2. Methods

2.1. Annotation of G. halophytocola GH sequences

The sequences of putative GHs and their respective CBMs were annotated from *G. halophytocola* (GenBank RefSeq Assembly ID: GCF_013179615.1) using dbCAN3 webserver [22]. Only annotations with a stringent e-value of e^{-30} were retained. The annotated GHs were subsequently filtered to select extracellular enzymes putatively involved in plant polysaccharide degradation, using the CAZy database as a functional reference (http://www.cazy.org, accessed on 30/11/2024). For each sequence, the presence of a signal peptide was predicted using SignalP 6.0 [23].

Three GH sequences belonging to polysaccharide-degrading families and containing predicted signal peptides were identified: GH13_30 (Gh_GH13_30, GenBank ID: WP_171919270), GH13_32 (Gh_GH13_32, GenBank ID: WP_309245053), and GH26 (Gh_GH26, UniProt ID: A0ABX5YB07). To assess their novelty and infer putative functions, their positions within the sequence space were analyzed. A 2D map for each family, including the *G. halophytocola* sequences, was generated using ProtSpace v2.1.2 (https://github.com/tsenoner/protspace [24]). Per-protein embeddings were computed using the encoder of the ProstT5_fp16 protein language model. Dimensionality reduction was performed via UMAP with default parameters (–n_neighbors 15 –min_dist 0.1), projecting the data into the first two dimensions.

Input sequences for the embedding space were retrieved by using each *G. halophytocola* sequence as a query to search for homologs in the UniRef30 + ColabFoldDB database (accessed 08/07/2025) via the MMseqs2 API within the *colabfold_search* script. The retrieved sequences were filtered to retain proteins with a length between 200 and 2000 amino acids, a minimum of 80% sequence coverage, and of 20% global identity to the query. Additionally, 97 characterized GH26 sequences listed in CAZy were included (http://www.cazy.org/GH26_characterized.html). To reduce redundancy, uncharacterized sequences were filtered to allow a maximum of 70% pairwise global sequence identity with the characterized sequences.

2.2. Structural modelling and substrate binding site conservation

The architecture and substrate specificity of Gh_GH26, preliminary inferred from sequence homology, were further investigated using a structure-based approach, to identify key substrate-binding residues. A 3D model was obtained using Boltz2 (https://github.com/jwohlwend/boltz [25]) by co-folding the Gh_GH26 sequence with oligosaccharides representative of GH26 family substrate specificities (2–6 moieties), including cello-oligosaccharides, β-1,3- and β-1,4-xylo-oligosaccharides, and manno-oligosaccharides. Substrates were generated in fully hydrogenated states using GLYCAM (https://glycam.org), manually verified with Avogadro v.1.2.0 [26], and converted to SMILES format using Open Babel v.3.1.0 [27].

Five diffusion samples were generated with default diffusion steps and ranked according to ipTM and affinity scores. Models were filtered using PoseBuster [28] to ensure chemical validity. Poses were retained only if they met specific catalytic criteria (<4 Å Euclidean distance between the catalytic nucleophile Oε and the attacked C_1, and the other between the catalytic acid/base Oε and the glycosidic O), ensuring a potentially catalytically competent conformation.

The best-ranked models meeting these thresholds underwent energy minimization and refinement via Molecular Dynamics (MD) simulations in an NPT ensemble. The MD protocol was adapted from the "Making it Rain" Colab Notebook https://colab.research.google.com/github/pablo-arantes/making-it-rain/blob/main/Protein_ligand.ipynb using Open MM v.7.7 [29] with ff19SB protein and OPC water forcefield models, as recommended in [30]. The protein catalytic residues were parametrized to ensure that the nucleophile Oε was deprotonated and the acid/base Oε protonated, to emulate the state of a retaining glycoside hydrolase reaction before the nucleophilic attack. Oligosaccharide was parameterized in Antechamber using sqm with the AM1-BCC charge model under the GAFF2 with modifications described in [31]. Specifically, a 10 Å padding was applied to the simulation box, ions were added only for neutralization, and equilibration consisted of a 2 ns NVT step at 298 K (Andersen thermostat, Verlet integrator) followed by a 2 ns NPT step. Heavy atoms of the enzyme and substrate were position-restrained (700 kJ/mol) during equilibration. Production MD simulations were performed in triplicate for 20 ns, starting from independent equilibration steps, with coordinates saved every 200 ps. System stability was monitored by calculating the heavy atom RMSD of the substrate against the protein backbone-aligned frames. Frames from the final 10 ns of each replicate were merged (100 frames per replicate) to analyze flexibility by heavy atom root mean square fluctuation (RMSF) and to identify stable protein-substrate non-covalent interactions. These interactions were assessed using proLIF interaction fingerprints [32] along MD simulations frames, using the default 6.0 Å threshold. Different fingerprints (involving different interaction types or different atoms) from the same residue were merged. The substrate binding residues were identified as those involved with an interaction fingerprint for >50% of MD frames. Those residues were compared to structurally aligned positions in homologous GH26s to inform on similarities and differences in the binding mode of the substrate.

2.3. Production and purification of recombinant Gh_GH26

The sequence coding for Gh_GH26, optimized for expression in *Escherichia coli* cells, was chemically synthesized (Genscript, Piscataway, NJ, USA) and cloned in frame with a C-terminal 6× His-Tag into the pET21 vector (EMD, Millipore, Billerica, MA, USA) between the *Nde*I and *Xho*I sites (Fig. S1). Site-directed mutagenesis was performed using the QuickChange® PCR method with primers and annealing conditions detailed in Table S1. Reactions employed Q5® High-Fidelity DNA Polymerase (New England BioLabs, Ipswich, MA, USA) and an Eppendorf Mastercycler (Eppendorf, Hamburg, Germany) using the following parameters: initial denaturation at 98 °C for 2 min; 25 cycles at 98 °C for 10 s, annealing at the specified temperature for 25 s, and extension at

72 °C for 3 min; followed by a final extension step at 72 °C for 3 min. Successful incorporation of mutations was confirmed by bidirectional DNA sequencing.

The pET21 [Gh_GH26] vector and its derivatives were used to transform *E. coli* BL21 (DE3). Recombinant Gh_GH26 was produced in Zym5052 medium [33] and purified as described previously [14]. Purified Gh_GH26 was buffer exchanged in a 25 mM sodium phosphate buffer (PB) at pH 7. Protein concentration was determined using the Bradford protein assay (Bio-Rad, California, USA) with bovine serum albumin as a standard.

2.4. Biochemical characterization of Gh_GH26

The substrate specificity of Gh_GH26 was determined using colorimetric substrates, pNP-β-D-glucopyranose, pNP-β-D-mannopyranose and pNP-β-D-xylopyranose (Merck, Darmstadt, Germany), and natural polysaccharides, guar galactomannan, tara galactomannan, low viscosity carob galactomannan (LVCG), ivory nut mannan, beechwood glucuronoxylan (Megazyme code: P-XYLNBE), tamarind xyloglucan (Megazyme code: P-XYGLN), wheat flour arabinoxylan (Megazyme code: P-WAXYL) and carboxymethylcellulose (VWR International Radnord, USA). Galactomannans polysaccharides were kindly provided by Dr. Erika Ponzini and were prepared as described in [34]. The reactions with nitrophenyl glycoside derivatives were carried out at 40 °C in 100 μL of PB at pH 7 with 0.5 mg/mL of enzyme and 10 mM of nitrophenyl glycoside derivatives. Reactions were stopped after 15 min by the addition of 100 μL 1 M Na_2CO_3 pH 11. The ΔAbs_{min} was measured at 405 nm (ε: 18.6 mM^{-1} cm^{-1}) with a VICTOR™ X Multilabel Plate Reader (PerkinElmer Inc., USA). Activity on polysaccharides was determined using the DNS assay as described [33]. 100 μL reactions containing 0.5% *w/v* polysaccharide and 0.15 mg/mL purified enzyme were performed in PB at 35 °C and 800 rpm in a thermal shaker (Eppendorf, Hamburg, Germany). The calibration curve was constructed using known concentrations of pure D-mannose to quantify released sugars (Fig. S2).

The optimal catalytic conditions and the effects of metal ions on Gh_GH26 activity were investigated using the colorimetric substrate azo-carob galactomannan (ACG, Megazyme) at 1% *w/v* concentration. Reactions were performed in a final volume of 100 μL and stopped after 2.5 min by adding 250 μL of 96% (*v/v*) ethanol. The denatured enzyme and polymeric ACG precipitate were removed by centrifugation at 3000*g* for 5 min at room temperature. The azo dye released into the supernatant was quantified by measuring the ΔAbs_{min} at 590 nm using the VICTOR™ X Multilabel Plate Reader. To convert absorbance into an equivalent amount of released sugars, a calibration curve was constructed by fitting the ΔAbs_{min} to the amount of released sugars measured by DNS assay from a reaction in the same conditions using LVCG and varying the enzyme concentration (0.05 to 0.3 mg/mL). Both reactions were stopped after 2.5 min.

The optimal pH for catalysis was measured in the pH range 3.0–10.0 in PBS buffer at 40 °C. The optimal temperature of catalysis (*Topt*) was recorded in the temperature range of 10–60 °C in ammonium acetate buffer 25 mM at pH 5.5. Kinetics parameters were determined using 0.15 mg/mL of enzyme with ACG at 45 °C in ammonium acetate buffer at pH 5.5.

2.5. Effect of sodium chloride and bivalent cations on the activity and stability of Gh_GH26

The effects of NaCl and bivalent cations on Gh_GH26 activity and stability were evaluated in ammonium acetate buffer at pH 5.5. NaCl impact on activity was assessed using ACG as substrate at 45 °C in the 0–2.5 M salt concentration range. Long-term thermal stability of Gh_GH26 (0.5 mg/mL) was monitored over 14 days of incubation at 45 °C by measuring activity on ACG with and without 2.5 M NaCl.

The influence of metal ions on Gh_GH26 activity was examined at 40 °C on 1% ACG in the presence of 1, 2.5, and 5 mM $CaCl_2$, $CoCl_2$, $MnCl_2$, $MgCl_2$, $NiSO_4$, $CuSO_4$, and $ZnCl_2$. Reactions were started by adding 0.15 mg/mL enzyme and monitored for 2.5 min, as above. Thermal unfolding was monitored in ammonium acetate buffer pH 5.5 by recording the CD ellipticity at 222 nm from 5 °C to 90 °C at a rate of 1 °C/min, both in the absence and in the presence of increasing NaCl concentrations (0–2.5 M) or 5 mM of the above metal ions. Enzyme concentration was 0.15 mg/mL. All experiments were performed in triplicate.

2.6. LVCG and MOS degradation pattern

The degradation of mannotetraose (Man4X), mannohexose (Man6X), and LVCG, was performed in ammonium acetate buffer at pH 5.5, in the presence of 10 g/L polysaccharide/oligosaccharide and Gh_GH26 (1 mg/mL), as described previously [14], with the following modifications: the reaction mixtures were incubated in a thermal shaker (Eppendorf, Hamburg, Germany) at 45 °C and 650 rpm for 2 h. After precipitation with 80% *v/v* acetonitrile in water and centrifugation at 13,000 ×*g*, the clarified supernatants were diluted with ultrapure water to a final acetonitrile concentration of 50% v/v and then analyzed using ultra-performance liquid chromatography separation coupled with high-resolution mass spectrometry (UPLC–HRMS). The UPLC–HRMS analysis was carried on a Xevo G2-XS quadrupole time of flight mass spectrometer coupled to a Waters ACQUITY UPLC H-Class system through an ESI source (Waters Corporation, Milford, MA, USA). Chromatographic separation was performed at room temperature on an XBridge BEH Amide Column 4.6 × 150 mm 3.5 μm (Waters, Milford, MA, USA) equipped with a Vanguard column. The mobile phase consisted of water (A) and acetonitrile containing 0.1% ammonia (B). Samples and standards (10 μL) were injected, and elution was performed using a linear gradient from 75% B to 45% B over 7.5 min, followed by 1 min at 45% B and a 17-minute re-equilibration to the initial conditions. The flow rate was maintained at 0.8 mL/min. Mass detection was conducted using an electrospray ionization source in the negative ion mode, with capillary and cone voltages set at 2 kV and 40 V, respectively. Analytical pure mannose (Man1X, *m/z* 179.05) and mannobiose (Man2X, m/z 341.1), Man4X (m/z 665.2) and Man6X (m/z 989.3) were used as a standard for retention time. Data acquisition was managed using Masslynx software v4.2 (Waters, Milford, MA, USA) and processed using OriginLab software (OriginLab Corporation, Northampton, MA, USA).

3. Results

3.1. The G. halophytocola CrR6 genome encodes a set of extracellular GHs, including an atypical GH26

The genome of *G. halophytocola* CrR6 (GenBank ID: GCA_013179615.1) was estimated to be 98.2% complete based on comparison with the phylogenetically related and complete assembly from G. *halophytocola* KLBMP_5180 (GenBank ID: GCA_001302565.1). 28 GHs were annotated, belonging to 16 different families (Fig. 1A). Among the seven GHs predicted to be secreted (identified by the presence of a signal peptide), three are associated with the degradation of disaccharides (a GH68 and two GH32 enzymes), one with the degradation of oligosaccharides (GH3) and three with the degradation of polysaccharides (GH13_30, GH13_32, GH26). We focused on the polysaccharide-degrading GHs, investigating their sequence, structure and functional diversity in relation to known GHs (Fig. 1B). GH13_30 and GH13_32 shared high similarity (>60% identity) to well-characterized enzymes in their respective families, suggesting a role in amylose chain depolymerization (Fig. S3). In contrast, GH26 is located in a sparsely characterized region, sharing 47.9% global sequence identity with the β-1,4-mannanse from *Cellulomonas fimi* (CfMan26A, Uniprot ID: Q9XCV5, [35]), while being evolutionarily distant from any other characterized GH26.

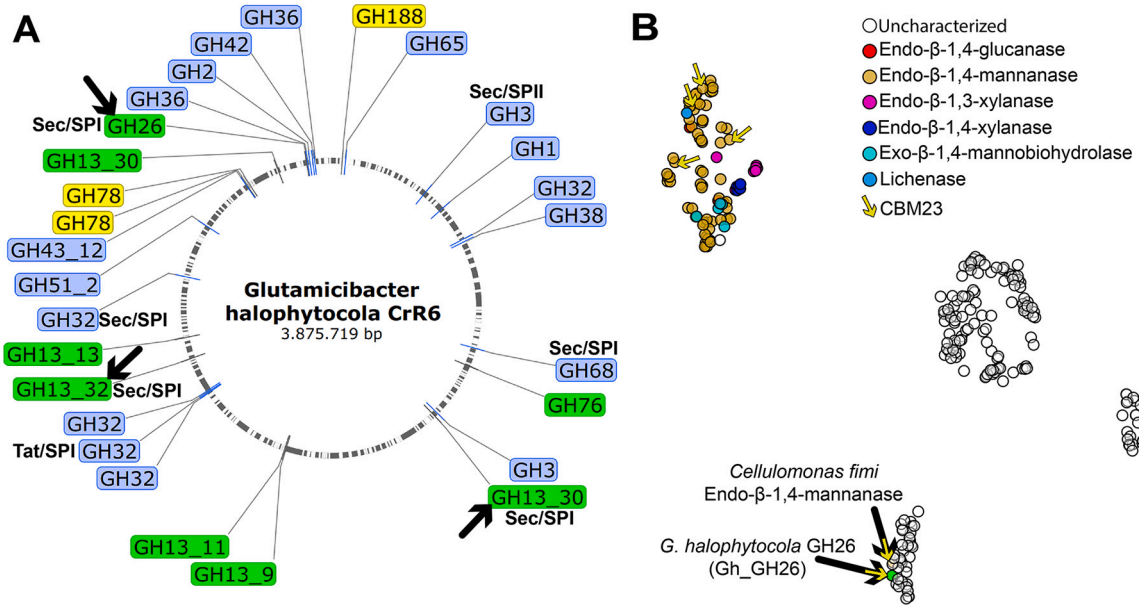

Fig. 1. Genomic annotation and sequence space of Gh_GH26. (A) Annotated glycoside hydrolases (GHs) encoded in the *G. halophytocola* CrR6 genome. Blue, GH families involved in disaccharide and oligosaccharide degradation; green, GH families involved in polysaccharide degradation; yellow, GH families involved in the degradation of sugar-containing composite biomolecules. Signal peptides are annotated as Sec/SPI or Sec/SPII. Black arrows indicate GH families acting on polysaccharides. (B) Two-dimensional UMAP projection of ProstT5_fp16 per-protein embeddings of Gh_GH26 together with 329 homologs sharing at least 20% global pairwise sequence identity, representing the combined structural, functional, and evolutionary sequence space of the GH26 family. Each circle represents a unique sequence. The 95 functionally characterized sequences from CAZy (accessed November 30, 2024) are color-coded according to their enzymatic activity. Yellow arrows indicate the characterized sequences containing a C-terminal CBM23 domain. The EC numbers associated with the reported activities are as follows: *endo*-β-1,4-glucanase (EC 3.2.1.4), endo-β-1,4-mannanase (EC 3.2.1.78), endo-β-1,3-xylanase/lichenase (EC 3.2.1.32), endo-β-1,4-xylanase (EC 3.2.1.-), and exo-1,4-β-mannobiohydrolase (EC 3.2.1.100).

Structural modelling and sequence analyses suggest that Gh_GH26 is a three-domain enzyme bearing an N-terminal signal peptide (1–28) for secretion. Its catalytic domain (29–415) exhibits the classical $(\alpha/\beta)_8$ TIM barrel fold and contains the conserved catalytic nucleophile residue E320 and acid-base residue E212. Gh_GH26 also comprises two β-sheet rich domains: a fibronectin-like domain (421–513) and a carbohydrate binding module (CBM) 23 domain (534–685). These two domains are connected by an unstructured linker (514–533, Fig. 2A). In contrast, the closest characterized enzyme CfMan26A (1010 AA) is a four-domain protein that carries an additional β-sheet rich domain with unknown function localized at the C-terminal with respect to CBM.

3.2. Bioinformatics analyses identify Gh_GH26 as an endo-β-mannanase with peculiar −3/−4 subsites

Substrate specificity of Gh_GH26 was inferred using a structure- and conservation-based computational approach. Among the various oligosaccharides co-folded in silico with Gh_GH26, only mannohexose (Man6X) adopted a catalytically competent binding mode, occupying subsites from −4 to +2 (Fig. 2B). Short MD simulations of the Gh_GH26-Man6X complex showed that Man6X moved similarly in all replicates within the first few ns, assuming a slightly different conformation at subsites −4, −3 and +2 (Figs. 2C and S5). However, the mannose units of Man6X at the core of the active site (subsites −1 and +1) remained within <1 Å of their initial positions. Catalytic distances remained consistent along the simulation and compatible with a retaining hydrolytic mechanism (Fig. 2C), common to GH26. Structural comparison of the Gh_GH26 substrate-binding site with that of CfMan26A showed a high degree of conservation for residues at subsites −2 to +1, except for E129. Subsite −3 contains the conserved aromatic residue (Y364) but lacks the CfMan26A L122 interacting with the opposite side of the D-mannose ring. Subsite −4 was unique to Gh_GH26 (Fig. S4). Comparison with the substrate-binding sites of other characterized GH26 *endo*-mannanases, confirmed the conservation of subsites −2 to +1, despite Q368 at subsite −1 is shared only with CfMan26A. Subsites −3 and − 4 exhibit no conservation at all and subsite +2 is present only in GH26s with a C-terminal CBM23 (Fig. 2C). Notably, the subsites −3 and −4 also display an average RMSF of ≈2–3 Å, which is higher than that of −2 to +1 subsites (Fig. 2C), suggesting that this increased flexibility translates to a lower contribution to substrate specificity.

3.3. Gh_GH26 is a mesophilic enzyme activated and stabilized by high NaCl concentrations

Recombinant Gh_GH26 was purified by metal-affinity chromatography (Fig. S6), yielding 5 mg pure protein/L of culture. Its substrate specificity was investigated using *ortho*- and *para*-nitrophenyl sugar derivatives and various polysaccharides representative of those typically found in plant extracellular matrices. Gh_GH26 was active only on branched and unbranched mannan-derived polysaccharides, with the highest specific activity observed for soluble LVCG (Table 1). Given the viscosity of natural mannan and galactomannan and the ease of use and sensitivity of soluble synthetic colorimetric substrates, ACG was used for biochemical characterization. Gh_GH26 was active in the pH range of 5.0 to 8.0, with an optimum at pH 5.5 (Fig. 3A), exhibited highest activity at 45 °C and retained <10% of its activity at 10 °C (Fig. 3B). Thermal denaturation experiments showed that the enzyme retained its native secondary structure up to 40 °C, with a melting temperature (T_m) of 47.8 ± 0.8 °C (gray line in Fig. 4A), corresponding to a difference between T_m and T_{opt} of 2.8 °C, consistent with the values typical of mesophilic enzymes [41]. Kinetics parameters were determined at optimal catalysis conditions showing that Gh_GH26 follows a Michaelis-Menten kinetics with a K_M of 2.6 ± 0.2 mg/mL and a k_{cat} of 130 s^{-1} (Fig. 3C).

The effects of salt were assessed by measuring activity on ACG in the presence of varying NaCl concentrations (0–2.5 M). In these experiments Gh_GH26 exhibits halophilic behavior, showing increased activity at high salt concentrations (Fig. 4B). Thermal stability analysis was

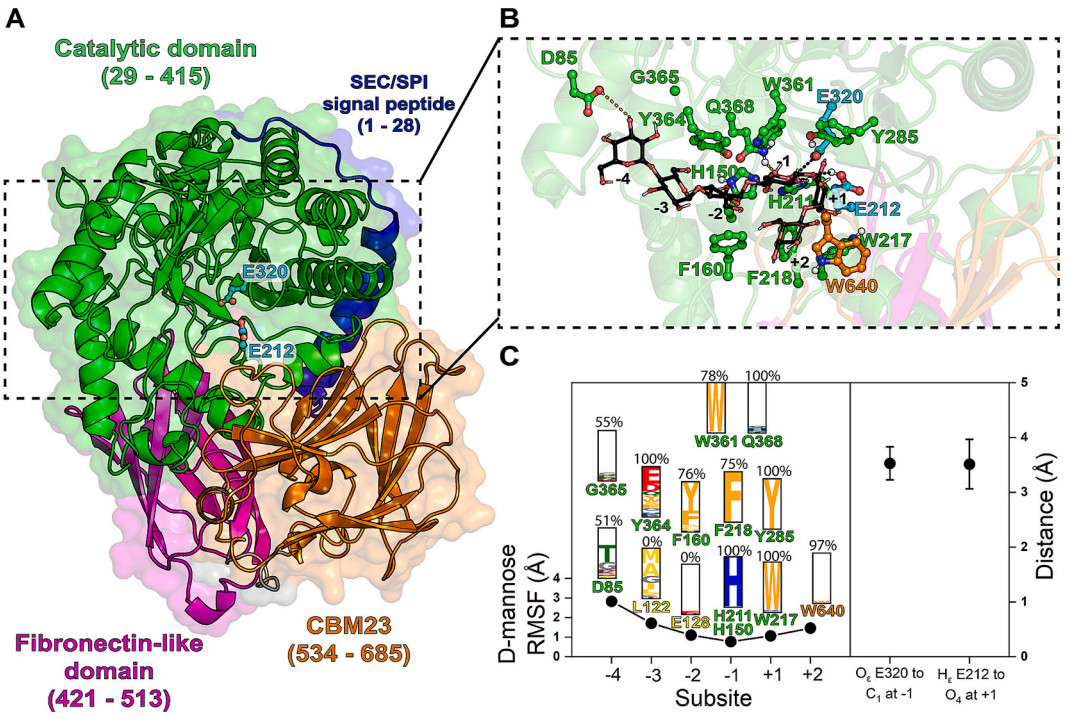

Fig. 2. Structural modelling and molecular dynamics simulations of Gh_GH26. (A) Cartoon representation of the Gh_GH26 structural model predicted by Boltz-2 in the absence of substrate. Side chains of catalytic residues are shown as ball-and-stick models, with carbon atoms in cyan and oxygen atoms in red. (B) Active site of Gh_GH26 in complex with Man6X. The substrate is shown as a stick model (carbon in black, oxygen in red, hydrogen atoms in white). The displayed conformation corresponds to a representative frame extracted after 10 ns of simulation. Subsites are labeled according to standard nomenclature. Key catalytic distances, from the nucleophilic Oε to the C1 atom at subsite −1 and from Oε to O4 at subsite +1, are indicated by black dashed lines. Residues of Gh_GH26 that maintain an interaction fingerprint with the substrate for more than 50% of the simulation time are shown as ball-and-stick models. Hydrogen bonds between the substrate and the protein are indicated by yellow dashed lines. (C) Molecular dynamics simulation statistics. Plots show per-subsite RMSF values of Man6X heavy atoms and the distribution of key catalytic distances. Gh_GH26 substrate-binding residues from panel B are highlighted in green, together with the relative amino acid frequencies derived from an alignment of 73 characterized GH26 endo-β-1,4-mannanases. Percentages above the bars indicate the fraction of simulation frames in which the corresponding Gh_GH26 residue exhibited any interaction fingerprint with the Man6X substrate at the corresponding subsite. Residues involved in substrate binding in CfMan26A (Fig. S4) are highlighted in yellow. Structural visualizations were generated using the open-source version of PyMOL 3.0.

Table 1
Gh_GH26 substrate specificity screening at pH 7 (sodium phosphate, NaP, buffer 25 mM) and 40 °C. An Enzymatic Unit (U) is defined as μmol D-mannose eq. released per minute. Values were averaged over three biological replicates and standard deviation was reported. ND: Not Detected.

Substrate	Specific activity (U/mg)
*p*NP-β-D-glucopyranose	ND
*p*NP-β-D-mannopyranose	ND
*p*NP-β-D-xylopyranose	ND
Guar galactomannan	9.9 ± 1.9
Tara galactomannan	8.3 ± 1.7
LVCG	41.9 ± 2.5
Ivory nut mannan	17.7 ± 3.7
Beechwood xylan	ND
Tamarind xyloglucan	ND
Wheat flour arabinoxylan	ND
Carboxymethylcellulose	ND

performed at the same NaCl concentrations, revealing a significant increase in T_m from 47.8 ± 0.8 °C at 0 M NaCl to 61.6 ± 1.1 °C at 2.5 M NaCl (Fig. 4A). The stabilizing effect of high salt concentration was also evident in kinetic stability assays. Gh_GH26 was incubated at 45 °C in the absence and presence of 2.5 M NaCl. Without NaCl, the enzyme was completely inactivated within 2 days, whereas under high salt conditions, it retained activity for up to 14 days (Fig. 4C).

3.4. Gh_GH26 efficiently hydrolyzes medium- to long-chain MOS

To elucidate the hydrolytic mechanisms of Gh_GH26, the degradation products of the enzymatic hydrolysis of Man4X, Man6X, and LVCG were analyzed by UPLC-HRMS. It should be noted that this technique does not allow absolute quantification of released MOS as peak intensity depends not only on their concentration but also on the ionization efficiency of each MOS during electrospray ionization. As shown in Fig. S7, the standards Man1X, Man2X, Man4X, and Man6X analyzed at the same concentration (0.5 mg/mL) exhibit different peak intensities. Therefore, the analysis focused exclusively on the degradation pathway rather than the quantity of MOS produced.

Incubation of Man4X with Gh_GH26 for 2 h led to ~80% hydrolysis, yielding Man2X and Man3×, whereas Man1X was not detectable (Fig. 5A). The absence of Man1X, despite its ionization efficiency is comparable to that of Man2X, indicated that Man2X is the primary product. The apparent abundance of Man3× may be overestimated because of its higher ionization efficiency. In contrast, Man6X was completely hydrolyzed after 2 h of incubation, releasing Man2X, Man3X, and Man4X (Fig. 5B), showing that Gh_GH26 preferentially acts on longer-chain oligosaccharides.

Analysis of the LVCG degradation products provided similar results. After 2 h of incubation, the enzyme primarily released medium-chain MOS with lengths ranging from 3× to 7× (Fig. 5C). Extended incubation (24 h) led to the degradation of high molecular weight MOS, resulting in predominantly Man3X and Man4X peaks, and low intensity peaks of mannose (Man1X) and mannobiose (Man2X, Fig. 5C). Unfortunately, UPLC-HRMS does not distinguish branched and unbranched

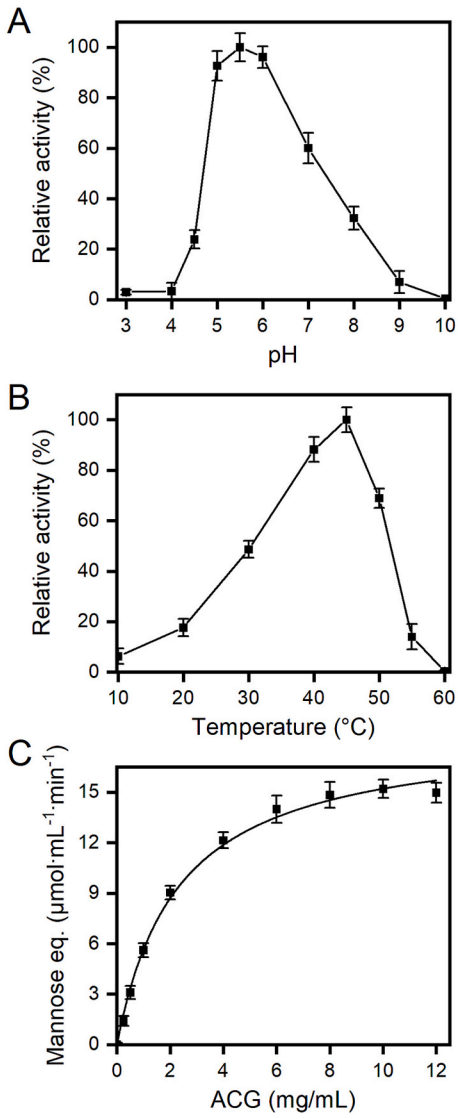

Fig. 3. Biochemical characterization of Gh_GH26. The effects of pH (A) and temperature (B) on the activity of Gh_GH26. Reactions were carried out using ACG (1% *w/v*) as the substrate. (C) Steady-state kinetics of Gh_GH26 on ACG under optimal conditions.

oligosaccharides, as mannose and galactose have identical molecular weights. However, the Man4X and Man6X peaks eluted at the same volume as the linear standards (Fig. S7), suggesting that they are unbranched products.

Overall, these results indicate that Gh_GH26 acts as an *endo*-mannanase, requiring substrates with a degree of polymerization of at least four sugar moieties and exhibiting higher catalytic efficiency towards longer MOS. The hydrolytic pattern of Gh_GH26 suggests the presence of up to four substrate-binding subsites on the non-reducing side of the catalytic center (−1 to −4), although the enzyme appears to preferentially accommodate the substrate across the +3 to −3 subsites. These observations are consistent with in silico predictions, which identified a catalytically competent binding mode for Man6X only.

3.5. Ca^{2+} activates and stabilizes the enzyme at mM concentrations, and its binding site is conserved among GH26s

The effects of divalent cations (Ca^{2+}, Mg^{2+}, Mn^{2+}, Co^{2+}, Zn^{2+}) on the activity and stability of Gh_GH26 were evaluated by measuring enzyme activity at metal ion concentrations ranging from 0 to 5 mM and

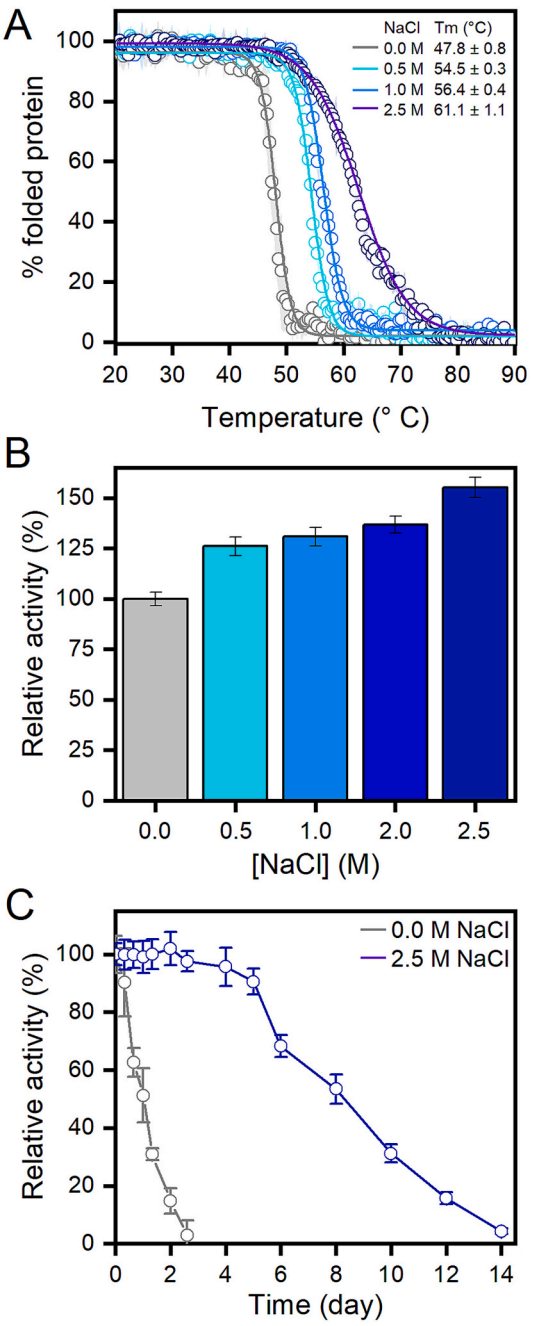

Fig. 4. Effect of NaCl on the activity and stability of Gh_GH26. (A) Thermal stability of Gh_GH26 at increasing NaCl concentrations, measured by monitoring the CD signal at 222 nm. (B) Relative activity on 1% (*w/v*) ACG at different NaCl concentrations. (C) Kinetic stability of Gh_GH26 determined by measuring residual activity after incubation at 45 °C with and without 2.5 M NaCl. Experiments were performed in triplicate, and the error bars indicate standard deviations ($n = 3$).

assessing thermal stability through thermal ramp analysis in the presence of 5 mM of each ion. The activity of Gh_GH26 was significantly enhanced by Ca^{2+}, with the highest increase (80%) recorded at 5 mM $CaCl_2$ (Fig. 6A). Furthermore, the presence of 5 mM $CaCl_2$ increased the T_m of Gh_GH26 from 47.8 ± 0.8 °C to 52.4 ± 1.1 °C (Fig. 6B). Mg^{2+} and Mn^{2+} slightly improved the enzyme activity without affecting its thermal stability (Fig. 6A and B), while Co^{2+} and Zn^{2+} negatively impacted both the enzyme activity and thermal stability (Fig. 6A and B). Taken together results suggested that Ca^{2+} interacts with Gh_GH26 and that activation may result from interaction-driven stabilization. Steady-state

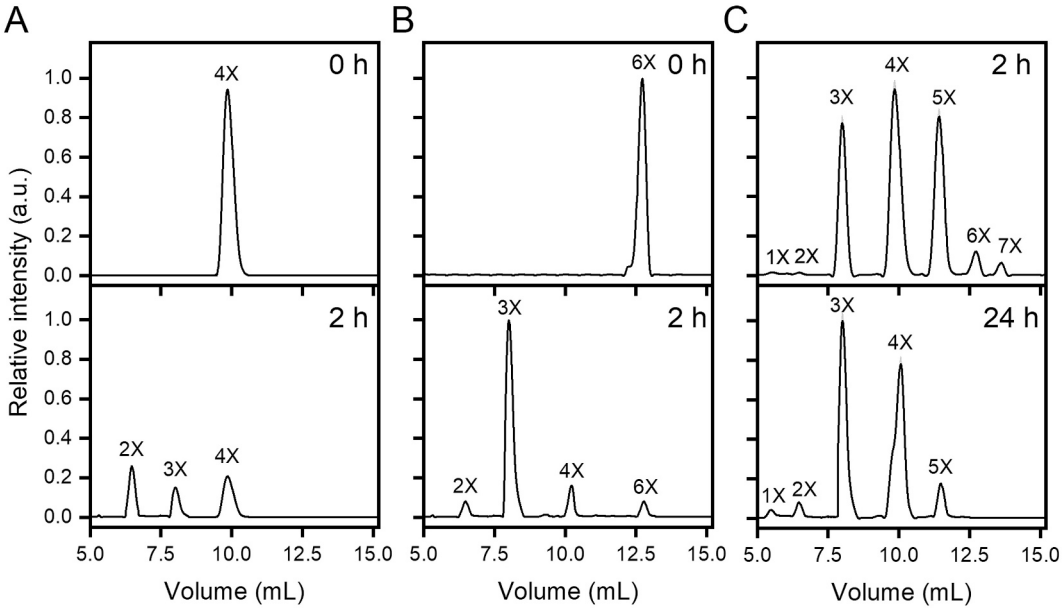

Fig. 5. Degradation of MOS and soluble LVCG. Linear Man4X (A) and Man6X (B) were incubated with 0.5 mg/mL Gh_GH26 in ammonium acetate buffer at 45 °C for 2 h. (C) Soluble LVCG was degraded under similar conditions for 2 and 24 h. Reactions were stopped by boiling, and the clarified supernatant was cold-precipitated with ultrapure acetonitrile. The degradation products were analyzed by UPLC-MS. One representative chromatogram out of three independent replicates is shown.

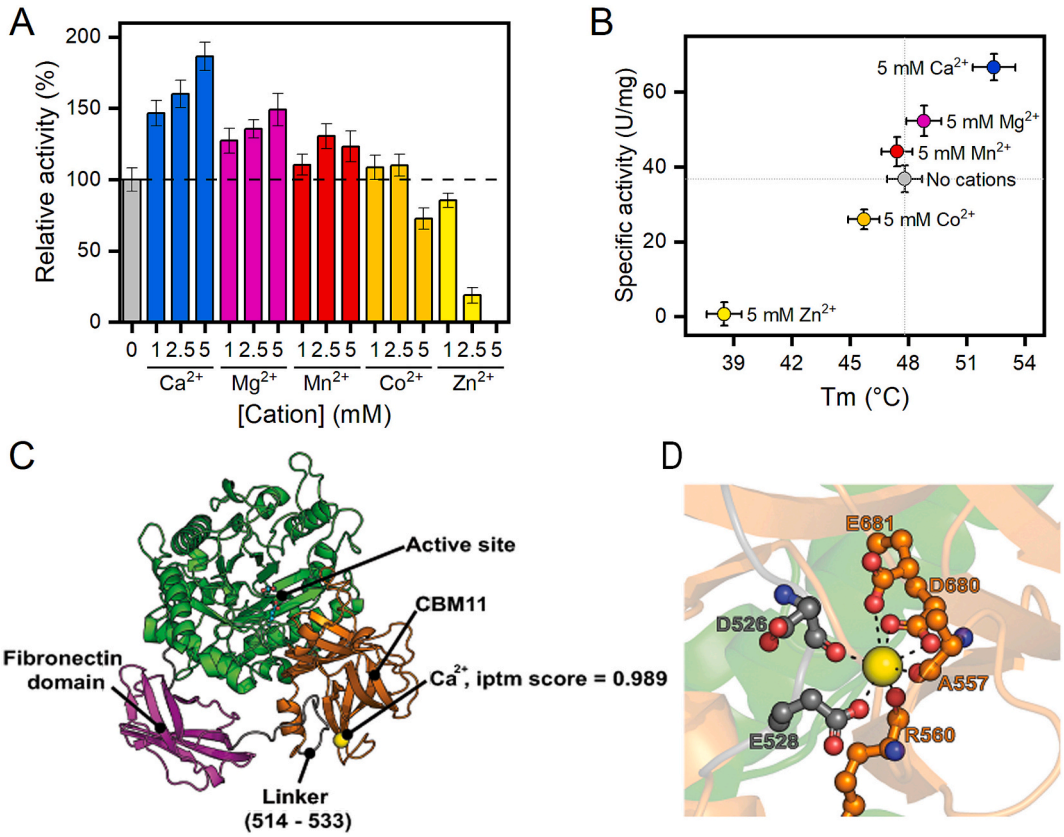

Fig. 6. Effect of divalent cations on the activity and stability of Gh_GH26. (A) Relative activity of Gh_GH26 in the absence (gray bar) and in the presence of different cations concentrations. Reactions were carried out using ACG (1% w/v) as the substrate. (B) Relationship between the Tm and specific activity of Gh_GH26 recorded in the absence and in the presence of 5 mM cations. (C) A Boltz-2 co-folding model of Gh_GH26 and a Ca^{2+} ion visualized in cartoon form. (D) A zoom of the putative Ca^{2+} binding site. Residues involved in Ca^{2+} coordination are highlighted with ball-and-stick models, and putative non-covalent interactions are indicated by black dashed lines. Experiments were performed in triplicate, and error bars indicate standard deviations (n = 3). Visualizations were obtained with open-source PyMOL 3.0.

Michaelis–Menten kinetics measured in the presence of 0, 2.5, and 5 mM Ca^{2+} revealed no significant differences in K_M indicating that Ca^{2+} does not measurably affect substrate-binding affinity (Fig. S8), suggesting that Ca^{2+} may primarily affects catalytic efficiency by modulating protein dynamics.

The putative Ca^{2+} binding site was predicted by combining Boltz-2 co-folding [25] and AllMetal3D [36]. The latter is a deep learning method that can discriminate between different metals and binding geometries. Both computational tools identified a Ca^{2+} binding site (ipTM score ≈ 0.99 and confidence score of 100% for AllMetal3D) within the CBM23 domain and the linker connecting it to the fibronectin domain (Fig. 6C). Boltz-2 models with other cations reported lower but confident ipTM metric for the same binding site. However, considering the Ca^{2+} effects on Gh_GH26, the subsequent analysis focused on this cation. The predicted Ca^{2+} binding site adopted a pentameric bipyramidal geometry (Fig. 6D) with the ion coordinated by E528-O_ε, both O_ε of D680, and by the backbone oxygen atoms of D526 and A557. Two vertices were formed by the backbone oxygen of R560 and E681-O_ε.

To experimentally validate this prediction, three variants were obtained by substituting E528, D680, and E681 with alanine. Their activity and stability were assessed in the absence and in the presence of 5 mM Ca^{2+}. Without Ca^{2+}, the activity and thermal stability of the Gh_GH26 variants were similar to those of the wild-type enzyme, except for E681A, which exhibited a slight decrease in activity, suggesting that the mutations did not affect the overall structure of the enzyme (Fig. S9 and Fig. 7B). The activity and stability of E528A and D680A variants were unaffected by the presence of Ca^{2+} (Fig. 7A and B), indicating that these two residues are involved in calcium coordination. In contrast, the E681A variant behaved similarly to the wild-type enzyme, suggesting that this residue may not be directly involved in ion coordination (Fig. 7A and B). A comparison between the CBM23 domain of Gh_GH26 and those of other characterized GH26s highlighted a strict conservation

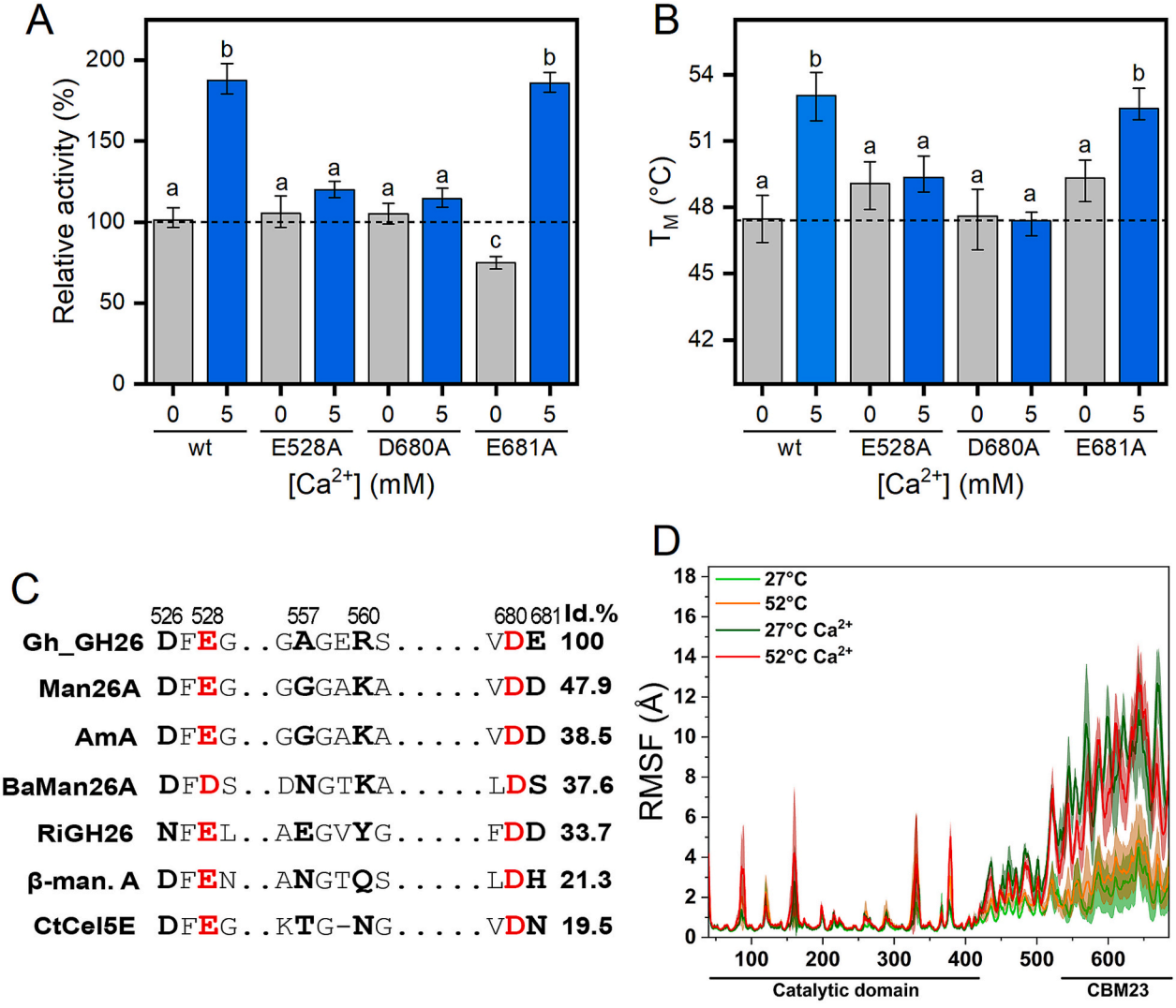

Fig. 7. Identification of the Ca^{2+} binding site. Relative activity (A) and T_m (B) of Gh_GH26 WT, E528A, E680A, and E681A variants in the absence and presence of 5 mM Ca^{2+}. Reactions were performed using ACG (1% w/v) as the substrate. The thermal stability was assessed as previously described. Different letters above the bars indicate statistically distinct groups: samples sharing the same letter (a, b, or c) are not significantly different, whereas samples with different letters differ significantly. Statistical analysis was performed using one-way ANOVA followed by Tukey's post-hoc test ($p < 0.05$). (C) Conservation of residues involved in Ca^{2+} binding among characterized GH26 homologs containing a C-terminal CBM23 or CBM11 domain. Man26A = *Cellulomonas fimi* GH26 (UniProt ID: Q9XCV5); AmA = *Bacillus* sp. JAM750 (UniProt ID: Q2ACI1); BaMan26A = *Bifidobacterium adolescentis* ATCC 15703 (GenBank ID: A1A278); RiGH26 = *Roseburia intestinalis* (UniProt ID: A0AAQ2U8W3); β-man. A = *Bacillus* sp. (GenBank ID: P16699); and CtCel5E = *Clostridium thermocellum* (GenBank ID: P16218). Id.% indicates global pairwise sequence identity. (D) RMSF profiles of the catalytic and CBM23 domains in the presence and absence of Ca^{2+} at different temperatures. RMSF values were calculated after superposition of all MD frames on the backbone atoms of the catalytic domain (residues 29–415). Mean values and standard deviations across three independent MD replicates (200–300 ns) are shown (Fig. S10). All reported values are averaged over three simulation replicates.

of residues D526, E528, and D680, except for RiGH26 from *Roseburia intestinalis* (Fig. 7C). These residues are also conserved in the CBM11 domain of *Clostridium thermocellum* CtCel5E, where they are involved in the coordination of Ca^{2+} ion [37]. Therefore, despite the low sequence identity between CBM11 and CBM23, our analyses indicate they share a highly conserved Ca^{2+} binding site.

To further investigate the possible mechanism underlying the effects of Ca^{2+} binding, unbiased MD simulations on Gh_GH26 were performed with and without the ion bound on the CBM23 domain, at two different temperatures (27 and 52 °C). Superimposition of the simulation frames (last 100 ns of 300 ns triplicates; Fig. S10) onto the N-terminal catalytic domain backbone showed that the RMSF of the CBM23 backbone significantly increased at both temperatures in the presence of Ca^{2+} (Fig. 7D). In contrast, the intra-domain motions within the CBM backbone remained largely unchanged by Ca^{2+}, exhibiting only minor temperature-dependent variations (Fig. S11). Taken together, these data indicate that Ca^{2+} enhances the flexibility of CBM23 relative to the rest of the enzyme, without affecting its intrinsic stability.

4. Discussion

G. halophytocola enhances salt tolerance in various plant species by producing exopolysaccharides that reduce sodium uptake [20,21,38]. Enzymes secreted by this strain are likely halophilic or halotolerant, making them promising candidates for biotechnological applications in high-salinity environments where non-halophilic enzymes are often ineffective [15,16].

Among secreted GH enzymes, this work focused on Gh_GH26, as it occupies a poorly explored region of the GH26 sequence space. This enzyme retains both activity and stability under high salt conditions, with high salt levels further enhancing its catalytic performance and thermal stability. Salt adaptation mechanisms in halophilic/halotolerant enzymes involve modifications on the protein surface, including a decrease in hydrophobic sites and an enrichment of negatively charged residues, which contribute to the formation of a stable ionic and hydration shell [39]. Analysis of the surface-exposed charged residues in the Boltz-2 model of Gh_GH26 revealed a marked excess of acidic residues. This feature has been previously associated with salt tolerance in other glycoside hydrolases [39]. This surface charge distribution appears to be independent of the presence of accessory domains, and it can be concluded that this is a common trait among salt-activated GH26 enzymes, irrespective of the salinity of their environments [40–44] (Table 2).

Sequence-based analysis indicated that Gh_GH26 occupies a distinct region of the GH26 sequence space, separate from the cluster containing most functionally characterized GH26 enzymes. Within this subgroup, Gh_GH26 is closely related only to the previously described homolog CfMan26A. Although the two enzymes differ in their overall domain architecture, both contain a CBM23 domain, a feature uncommon among characterized GH26s [45]. Indeed most GH26s either lack a CBM or are associated with one or more N-terminal CBM35 domains [46] (Fig. S12). The CBM23 domain belongs to the family of type B CBMs and adopts the characteristic β-sandwich fold, in which a concave surface forms the substrate-binding cleft [47]. This domain has been shown to bind mannan with low micromolar affinity and to enhance the activity of full-length Man26A on galactomannans relative to a CBM23-truncated construct [40]. However, no further structural or functional studies have investigated how CBM23 compares with other CBM families or clarified the potential role of metal ions in ligand recognition and substrate binding. Our structural analysis revealed that CBM23 is closely related to the CBM11 domain of CtCel5E, a multidomain GH containing both GH5 and GH26 catalytic modules. In CtCel5E, CBM11 mediates binding to β-1,3- and β-1,4-glucans and coordinates two Ca^{2+} ions [47,48], suggesting that metal coordination may also contribute to the structural stability and/or ligand-binding properties of CBM23. Sequence analysis showed that one of these two Ca^{2+} binding sites is conserved among the CBM23s of Gh_GH26 and other characterized GH26s (Fig. 7C). The strict conservation of the Ca^{2+} site, despite the marked divergence in the binding cleft, strongly suggests that ion-mediated structural stabilization is an ancestral feature predating the evolutionary diversification of these CBM families. Mutagenesis experiments highlighted the importance of Ca^{2+} coordination in enhancing both Gh_GH26 stability and activity. This effect is probably due to the ability of Ca^{2+} to regulate CBM flexibility and to modulate long-range interactions with the catalytic domain.

Gh_GH26 is an *endo*-mannanase that degrades LVCG into medium- and short-chain MOS. Although the analytical technique used in this study is qualitative rather than quantitative and cannot distinguish between branched and unbranched MOS, a plausible mechanism of action can be proposed. Conservation analysis indicates that the hallmark of the GH26 β-mannanase family is a highly conserved catalytic core centered on subsites −2 to +1. Consistent with a predicted substrate-binding cleft spanning subsites −4 to +2, Gh_GH26 efficiently degrades all MOS with a degree of polymerization >3, while showing no activity towards mannobiose (data not shown). This behavior aligns with previous studies on GH26 enzymes [46,49], where the conserved −1 and −2 subsites accommodate MOS regardless of α-galactosyl branches.

In contrast, subsites −3 and −4 show high variability across the family, dictating the specific product release patterns. Indeed, fungal GH26 enzymes typically feature a strong −4 subsite and release mainly Man1X and Man4X from Man5X [50,51], whereas *Bacteroides ovatus* BoMan26B utilizes a −5 subsite to convert Man6X primarily into Man1X and Man5X [51,52]. Conversely, enzymes lacking distal subsites, such as *Bacillus subtilis* BCman, exhibit negligible activity on short MOS [53]. A critical distinction is also observed between *Cellulomonas fimi* (CfMan26A) and *Cellvibrio japonicus* (CjMan26A): CfMan26A binds Man4X predominantly at subsites −3 to +1 (releasing Man1X and Man3X), while CjMan26A prefers subsites −2 to +2 (yielding mainly Man2X) [35,54,55].

Despite Gh_GH26 features a unique −4 subsite, the substrate binding residues at −3 (T362 and Y364) and −2 (Q368) subsites are similar to homologs A323, F325 and Q379 in CfMan26A (Fig. S4) [41]. This likely drives the release of Man3X and Man4X from carob galactomannan.

Table 2
Surface charge and NaCl tolerance of various GH26s. The analysis was performed by summing the number of charges from acidic (E and D, counted as −1 when deprotonated) and basic (R, H and K, counted as +1 when protonated) surface residues (>2.5 Å^2 of solvent-accessible area) whose protonation was assigned by pKa prediction of propka3.5.1 (https://github.com/jensengroup/propka) using as input Boltz-2-predicted 3D models without any signal peptide. Values in parentheses were calculated after removing accessory domains, if present. NA: Not Available.

Uniprot ID	Organism	Alophile	Measured effect at given NaCl concentration	Surface charge	Reference
A0ABX5YB07	*Glutamicibacter halophytocola*	Yes	Activity 50% higher, T_m 13 °C higher at 2.5 M	−20 (−11)	This study
I3PQX2	*Sphingomonas* sp. *JB13*	No	>85% Activity at 4.0 M	−2	[42]
A0A1S1YTI6	*Flammeovirga pacifica*	No	100% higher at 1.5 M	−9	[43]
B9VR69	*Bacillus velezensis H1*	Yes	100% higher at 4 M	−4	[44]
C0KZC5	*Pantoea agglomerans A021*	Moderate	>50% higher at 1 M	−3	[43]
Q9XCV5	*Cellulomonas fimi* ATCC 484	Yes	NA	−38 (−20)	[40]
P49424	*Cellvibrio japonicus*	No	NA	−3	[41]

However, the Man4X degradation profile suggests functional plasticity, allowing the enzyme to accommodate different binding modes. This plasticity may arise from two main structural features. First, Gh_GH26 lacks one interaction at subsite −3 (normally mediated by L122 in CfMan26A). Second, it features a major substitution at subsite −2, where a strictly conserved aromatic residue (W162 in CjMan26A, Y174 in CfMan26A) is replaced by D161. MD simulations of Man6X support this plasticity hypothesis, revealing high flexibility at subsites −3 and −4, which corresponds to reduced binding affinity in this distal region. Moreover, although the D161 at −2 did not form stable interactions during simulations, it clearly alters the local electrostatic environment.

In conclusion, insight into Gh_GH26 from the halophilic bacterium *G. halophytocola* broadens the current understanding of the structural and functional diversity within the GH26 family. The presence of a CBM23 domain is not merely a structural peculiarity of Gh_GH26, rather it provides a key functional advantage through a conserved Ca^{2+} coordination site that enhances both enzyme stability and activity. Further mechanistic studies on this Ca^{2+}-mediated stabilization, as well as into the specific binding preferences at the non-reducing end, will provide deeper structural insights. To successfully exploit this enzyme under industrial saline conditions, future efforts must transition from the model substrates analyzed in this study to the direct degradation of complex, untreated mannan-rich biomasses.

CRediT authorship contribution statement

Marco Orlando: Writing – review & editing, Writing – original draft, Visualization, Validation, Software, Methodology, Investigation, Formal analysis, Data curation, Conceptualization. **Mattia Salvadori:** Visualization, Investigation, Formal analysis. **Panagiotis F. Sarris:** Writing – review & editing, Supervision. **Marco Mangiagalli:** Writing – review & editing, Writing – original draft, Supervision, Conceptualization. **Marina Lotti:** Writing – review & editing, Supervision, Funding acquisition, Conceptualization.

Declaration of competing interest

The authors declare the following financial interests/personal relationships which may be considered as potential competing interests: Marina Lotti reports financial support was provided by European Commission. Marco Orlando reports financial support was provided by European Commission. If there are other authors, they declare that they have no known competing financial interests or personal relationships that could have appeared to influence the work reported in this paper.

Acknowledgements

Authors wish to thank Alessandro Marchetti for performing preliminary analyses, and Dr. Maura Brioschi, who carried out the UPLC–HRMS analyses and for her valuable contributions to the interpretation of the UPLC–HRMS results.

This work was supported by the University of Milano-Bicocca with FA (Fondo di Ateneo) to and by the European Cooperation in Science and Technology (COST Action: CA21162, COZYME) to M.L. M.O was supported by a postdoctoral fellowship from the University of Milano-Bicocca. This publication is co-funded by the European Union's Horizon Europe research and innovation program under the Marie Sklodowska-Curie COFUND Postdoctoral Programme grant agreement No.101081355-SMASH and by the Republic of Slovenia and the European Union from the European Regional Development Fund.

Appendix A. Supplementary data

Supplementary data to this article can be found online at https://doi.org/10.1016/j.ijbiomac.2026.154004.

Data availability

Data will be made available on request.

References

[1] M. Yamabhai, S. Sak-Ubol, W. Srila, D. Haltrich, Mannan biotechnology: from biofuels to health, Crit. Rev. Biotechnol. 36 (2016) 32–42, https://doi.org/10.3109/07388551.2014.923372.
[2] L.D. Melton, B.G. Smith, R. Ibrahim, R. Schröder, Mannans in primary and secondary plant cell walls, N. Z. J. For. Sci. 39 (2009) 153–160.
[3] I. Beidler, C.S. Robb, S. Vidal-Melgosa, M.-K. Zühlke, D. Bartosik, V. Solanki, S. Markert, D. Becher, T. Schweder, J.-H. Hehemann, Marine bacteroidetes use a conserved enzymatic cascade to digest diatom β-mannan, ISME J. 17 (2023) 276–285, https://doi.org/10.1038/s41396-022-01342-4.
[4] S. Vidal-Melgosa, A. Sichert, T.B. Francis, D. Bartosik, J. Niggemann, A. Wichels, W.G.T. Willats, B.M. Fuchs, H. Teeling, D. Becher, T. Schweder, R. Amann, J.-H. Hehemann, Diatom fucan polysaccharide precipitates carbon during algal blooms, Nat. Commun. 12 (2021) 1150, https://doi.org/10.1038/s41467-021-21009-6.
[5] H. Chanzy, M. Dube, R.H. Marchessault, J.F. Revol, Single crystals and oriented crystallization of ivory nut mannan, Biopolymers 18 (1979) 887–898, https://doi.org/10.1002/bip.1979.360180410.
[6] K. Katsuraya, K. Okuyama, K. Hatanaka, R. Oshima, T. Sato, K. Matsuzaki, Constitution of konjac glucomannan: chemical analysis and 13C NMR spectroscopy, Carbohydr. Polym. 53 (2003) 183–189, https://doi.org/10.1016/S0144-8617(03)00039-0.
[7] T. Hannuksela, C. Hervé du Penhoat, NMR structural determination of dissolved O-acetylated galactoglucomannan isolated from spruce thermomechanical pulp, Carbohydr. Res. 339 (2004) 301–312, https://doi.org/10.1016/j.carres.2003.10.025.
[8] E. Drula, M.-L. Garron, S. Dogan, V. Lombard, B. Henrissat, N. Terrapon, The carbohydrate-active enzyme database: functions and literature, Nucleic Acids Res. 50 (2022) D571–D577, https://doi.org/10.1093/nar/gkab1045.
[9] L. Reisky, A. Préchoux, M.-K. Zühlke, M. Bäumgen, C.S. Robb, N. Gerlach, T. Roret, C. Stanetty, R. Larocque, G. Michel, T. Song, S. Markert, F. Unfried, M. D. Mihovilovic, A. Trautwein-Schult, D. Becher, T. Schweder, U.T. Bornscheuer, J.-H. Hehemann, A marine bacterial enzymatic cascade degrades the algal polysaccharide ulvan, Nat. Chem. Biol. 15 (2019) 803–812, https://doi.org/10.1038/s41589-019-0311-9.
[10] L.R.S. Moreira, E.X.F. Filho, An overview of mannan structure and mannan-degrading enzyme systems, Appl. Microbiol. Biotechnol. 79 (2008) 165–178, https://doi.org/10.1007/s00253-008-1423-4.
[11] X. Huang, J. Lin, X. Ye, G. Wang, Molecular characterization of a thermophilic and salt- and alkaline-tolerant xylanase from Planococcus sp. SL4, a strain isolated from the sediment of a soda lake, J. Microbiol. Biotechnol. 25 (2015) 662–671, https://doi.org/10.4014/jmb.1408.08062.
[12] S. Titapoka, S. Keawsompong, D. Haltrich, S. Nitisinprasert, Selection and characterization of mannanase-producing bacteria useful for the formation of prebiotic manno-oligosaccharides from copra meal, World J. Microbiol. Biotechnol. 24 (2008) 1425–1433, https://doi.org/10.1007/s11274-007-9627-9.
[13] S.-J. Yoon, D.-C. Chu, L. Raj Juneja, Chemical and physical properties, safety and application of partially hydrolized guar gum as dietary fiber, J. Clin. Biochem. Nutr. 42 (2008) 1–7, https://doi.org/10.3164/jcbn.2008001.
[14] A. Marchetti, M. Orlando, S. Digiovanni, C. Christakis, V. Tsopanakis, N. Arapitsas, I.V. Pavlidis, P. Sarris, M. Mangiagalli, M. Lotti, Xylan degradation in the halotolerant bacterium *Bacillus altitudinis* relies on glycosidic hydrolases from families 11 and 30, J. Agric. Food Chem. 73 (2025) 27599–27610, https://doi.org/10.1021/acs.jafc.5c06247.
[15] S. DasSarma, P. DasSarma, Halophiles and their enzymes: negativity put to good use, Curr. Opin. Microbiol. 25 (2015) 120–126, https://doi.org/10.1016/j.mib.2015.05.009.
[16] Y.-K. Cen, L. Zhang, M.-P. Liu, C. Xiang, T.-X. Lu, Y.-P. Xue, Y.-G. Zheng, Salt-driven dynamic folding of halophile-origin enzymes: insights into evolution and protein exploitation, Int. J. Biol. Macromol. 302 (2025) 140527, https://doi.org/10.1016/j.ijbiomac.2025.140527.
[17] L. Reang, S. Bhatt, R.S. Tomar, K. Joshi, S. Padhiyar, U.M. Vyas, J.K. Kheni, Plant growth promoting characteristics of halophilic and halotolerant bacteria isolated from coastal regions of Saurashtra Gujarat, Sci. Rep. 12 (2022) 4699, https://doi.org/10.1038/s41598-022-08151-x.
[18] J.A. Barajas González, Y.E.K. de la Rosa, R. Carrillo-González, Ma. del C.Á. González-Chávez, M.E. Hidalgo Lara, R.M. Soto Hernández, B.E. Herrera Cabrera, NaCl modifies biochemical traits in bacterial endophytes isolated from halophytes: towards salinity stress mitigation using consortia, Plants (Basel, Switzerland) 13 (2024) 1626, https://doi.org/10.3390/plants13121626.
[19] N. Ben Amor, K. Ben Hamed, A. Debez, C. Grignon, C. Abdelly, Physiological and antioxidant responses of the perennial halophyte Crithmum maritimum to salinity, Plant Sci. 168 (2005) 889–899, https://doi.org/10.1016/j.plantsci.2004.11.002.
[20] C.A. Christakis, G. Daskalogiannis, A. Chatzaki, E.A. Markakis, G. Mermigka, A. Sagia, G.F. Rizzo, V. Catara, I. Lagkouvardos, D.J. Studholme, P.F. Sarris, Endophytic bacterial isolates from halophytes demonstrate phytopathogen biocontrol and plant growth promotion under high salinity, Front. Microbiol. 12 (2021) 681567, https://doi.org/10.3389/fmicb.2021.681567.

[21] W.-W. Feng, T.-T. Wang, J.-L. Bai, P. Ding, K. Xing, J.-H. Jiang, X. Peng, S. Qin, Glutamicibacter halophytocola sp. nov., an endophytic actinomycete isolated from the roots of a coastal halophyte, Limonium sinense, Int. J. Syst. Evol. Microbiol. 67 (2017) 1120–1125, https://doi.org/10.1099/ijsem.0.001775.
[22] J. Zheng, Q. Ge, Y. Yan, X. Zhang, L. Huang, Y. Yin, dbCAN3: automated carbohydrate-active enzyme and substrate annotation, Nucleic Acids Res. 51 (2023) W115–W121, https://doi.org/10.1093/nar/gkad328.
[23] F. Teufel, J.J. Almagro Armenteros, A.R. Johansen, M.H. Gíslason, S.I. Pihl, K. D. Tsirigos, O. Winther, S. Brunak, G. von Heijne, H. Nielsen, SignalP 6.0 predicts all five types of signal peptides using protein language models, Nat. Biotechnol. 40 (2022) 1023–1025, https://doi.org/10.1038/s41587-021-01156-3.
[24] T. Senoner, T. Olenyi, M. Heinzinger, A. Spannagl, G. Bouras, B. Rost, I. Koludarov, ProtSpace: a tool for visualizing protein space, J. Mol. Biol. 437 (2025) 168940, https://doi.org/10.1016/j.jmb.2025.168940.
[25] S. Passaro, G. Corso, J. Wohlwend, M. Reveiz, S. Thaler, V.R. Somnath, N. Getz, T. Portnoi, J. Roy, H. Stark, D. Kwabi-Addo, D. Beaini, T. Jaakkola, R. Barzilay, Boltz-2: Towards Accurate and Efficient Binding Affinity Prediction, 2025, https://doi.org/10.1101/2025.06.14.659707.
[26] M.D. Hanwell, D.E. Curtis, D.C. Lonie, T. Vandermeersch, E. Zurek, G.R. Hutchison, Avogadro: an advanced semantic chemical editor, visualization, and analysis platform, J. Cheminform. 4 (2012) 17, https://doi.org/10.1186/1758-2946-4-17.
[27] N.M. O'Boyle, M. Banck, C.A. James, C. Morley, T. Vandermeersch, G. R. Hutchison, Open babel: an open chemical toolbox, J. Chem. 3 (2011) 33, https://doi.org/10.1186/1758-2946-3-33.
[28] M. Buttenschoen, G.M. Morris, C.M. Deane, PoseBusters: AI-based docking methods fail to generate physically valid poses or generalise to novel sequences, Chem. Sci. 15 (2024) 3130–3139, https://doi.org/10.1039/D3SC04185A.
[29] P. Eastman, J. Swails, J.D. Chodera, R.T. McGibbon, Y. Zhao, K.A. Beauchamp, L.-P. Wang, A.C. Simmonett, M.P. Harrigan, C.D. Stern, R.P. Wiewiora, B.R. Brooks, V.S. Pande, OpenMM 7: rapid development of high performance algorithms for molecular dynamics, PLoS Comput. Biol. 13 (2017) e1005659, https://doi.org/10.1371/journal.pcbi.1005659.
[30] C. Tian, K. Kasavajhala, K.A.A. Belfon, L. Raguette, H. Huang, A.N. Migues, J. Bickel, Y. Wang, J. Pincay, Q. Wu, C. Simmerling, ff19SB: amino-acid-specific protein backbone parameters trained against quantum mechanics energy surfaces in solution, J. Chem. Theory Comput. 16 (2020) 528–552, https://doi.org/10.1021/acs.jctc.9b00591.
[31] M. Orlando, A. Marchetti, L. Bombardi, M. Lotti, S. Fusco, M. Mangiagalli, Polysaccharide degradation in an Antarctic bacterium: discovery of glycoside hydrolases from remote regions of the sequence space, Int. J. Biol. Macromol. 299 (2025) 140113, https://doi.org/10.1016/j.ijbiomac.2025.140113.
[32] C. Bouysset, S. Fiorucci, Prolif: a library to encode molecular interactions as fingerprints, J. Cheminform. 13 (2021) 72, https://doi.org/10.1186/s13321-021-00548-6.
[33] F.W. Studier, Protein production by auto-induction in high-density shaking cultures, Protein Expr. Purif. 41 (2005) 207–234, https://doi.org/10.1016/j.pep.2005.01.016.
[34] E. Ponzini, A. Natalello, F. Usai, M. Bechmann, F. Peri, N. Müller, R. Grandori, Structural characterization of aerogels derived from enzymatically oxidized galactomannans of fenugreek, sesbania and guar gums, Carbohydr. Polym. 207 (2019) 510–520, https://doi.org/10.1016/j.carbpol.2018.11.100.
[35] J. Le Nours, L. Anderson, D. Stoll, H. Stålbrand, L. Lo Leggio, The structure and characterization of a modular endo-β-1,4-mannanase from *Cellulomonas fimi*, Biochemistry 44 (2005) 12700–12708, https://doi.org/10.1021/bi050779v.
[36] S.L. Dürr, U. Rothlisberger, AllMetal3D: Joint Prediction of Localization, Identity and Coordination Geometry of Common Metal Ions in Proteins, 2025, https://doi.org/10.1101/2025.02.05.636627.
[37] A. Viegas, J. Sardinha, F. Freire, D.F. Duarte, A.L. Carvalho, C.M.G.A. Fontes, M. J. Romão, A.L. Macedo, E.J. Cabrita, Solution structure, dynamics and binding studies of a family 11 carbohydrate-binding module from *Clostridium thermocellum* (*Ct* CBM11), Biochem. J. 451 (2013) 289–300, https://doi.org/10.1042/BJ20120627.
[38] R. Hidri, O. Metoui-Ben Mahmoud, W. Zorrig, R. Azcon, C. Abdelly, A. Debez, The halotolerant rizhobacterium *Glutamicibacter* sp. alleviates salt impact on *Phragmites australis* by producing exopolysaccharides and limiting plant sodium uptake, Plant Direct 7 (2023) e535, https://doi.org/10.1002/pld3.535.
[39] L. Cao, R. Zhang, J. Zhou, Z. Huang, Biotechnological aspects of salt-tolerant xylanases: a review, J. Agric. Food Chem. 69 (2021) 8610–8624, https://doi.org/10.1021/acs.jafc.1c03192.
[40] D. Stoll, A. Boraston, H. StÃ¥lbrand, B.W. McLean, D.G. Kilburn, R.A.J. Warren, Mannanase Man26A from *Cellulomonas fimi* has a mannan-binding module, FEMS Microbiol. Lett. 183 (2000) 265–269, https://doi.org/10.1111/j.1574-6968.2000.tb08969.x.
[41] O. Hekmat, L. Lo Leggio, A. Rosengren, J. Kamarauskaite, K. Kolenova, H. Stålbrand, Rational engineering of mannosyl binding in the distal glycone subsites of *Cellulomonas fimi* endo-β-1,4-mannanase: mannosyl binding promoted at subsite −2 and demoted at subsite −3, Biochemistry 49 (2010) 4884–4896, https://doi.org/10.1021/bi100097f.
[42] J. Zhou, R. Zhang, Y. Gao, J. Li, X. Tang, Y. Mu, F. Wang, C. Li, Y. Dong, Z. Huang, Novel low-temperature-active, salt-tolerant and proteases-resistant endo-1,4-β-mannanase from a new Sphingomonas strain, J. Biosci. Bioeng. 113 (2012) 568–574, https://doi.org/10.1016/j.jbiosc.2011.12.011.
[43] Z.W. Cai, H.H. Ge, Z.W. Yi, R.Y. Zeng, G.Y. Zhang, Characterization of a novel psychrophilic and halophilic β-1, 3-xylanase from deep-sea bacterium, Flammeovirga pacifica strain WPAGA1, Int. J. Biol. Macromol. 118 (2018) 2176–2184, https://doi.org/10.1016/j.ijbiomac.2018.07.090.
[44] H. Djelid, S. Flahaut, Y. Oudjama, C.V. Wauven, N. Kacem Chaouche, High NaCl concentrations induce the resistance to thermal denaturation of an extremely halotolerant (salt-activated) β-mannanase from Bacillus velezensis H1, World J. Microbiol. Biotechnol. 39 (2023) 304, https://doi.org/10.1007/s11274-023-03754-6.
[45] Y. Hatada, N. Takeda, K. Hirasawa, Y. Ohta, R. Usami, Y. Yoshida, W.D. Grant, S. Ito, K. Horikoshi, Sequence of the gene for a high-alkaline mannanase from an alkaliphilic Bacillus sp. strain JAMB-750, its expression in Bacillus subtilis and characterization of the recombinant enzyme, Extremophiles 9 (2005) 497–500, https://doi.org/10.1007/s00792-005-0460-5.
[46] G.S. Kaira, M. Kapoor, Molecular advancements on over-expression, stability and catalytic aspects of endo-β-mannanases, Crit. Rev. Biotechnol. 41 (2021) 1–15, https://doi.org/10.1080/07388551.2020.1825320.
[47] A.L. Carvalho, A. Goyal, J.A.M. Prates, D.N. Bolam, H.J. Gilbert, V.M.R. Pires, L.M. A. Ferreira, A. Planas, M.J. Romão, C.M.G.A. Fontes, The family 11 carbohydrate-binding module of clostridium thermocellum Lic26A-Cel5E accommodates β-1,4- and β-1,3–1,4-mixed linked glucans at a single binding site, J. Biol. Chem. 279 (2004) 34785–34793, https://doi.org/10.1074/jbc.M405867200.
[48] D.O. Ribeiro, A. Viegas, V.M.R. Pires, J. Medeiros-Silva, P. Bule, W. Chai, F. Marcelo, C.M.G.A. Fontes, E.J. Cabrita, A.S. Palma, A.L. Carvalho, Molecular basis for the preferential recognition of β1,3-1,4-glucans by the family 11 carbohydrate-binding module from *Clostridium thermocellum*, FEBS J. 287 (2020) 2723–2743, https://doi.org/10.1111/febs.15162.
[49] L.E. Tailford, V.M.-A. Ducros, J.E. Flint, S.M. Roberts, C. Morland, D.L. Zechel, N. Smith, M.E. Bjørnvad, T.V. Borchert, K.S. Wilson, G.J. Davies, H.J. Gilbert, Understanding how diverse β-mannanases recognize heterogeneous substrates, Biochemistry 48 (2009) 7009–7018, https://doi.org/10.1021/bi900515d.
[50] P. von Freiesleben, O.V. Moroz, E. Blagova, M. Wiemann, N. Spodsberg, J. W. Agger, G.J. Davies, K.S. Wilson, H. Stålbrand, A.S. Meyer, K.B.R.M. Krogh, Crystal structure and substrate interactions of an unusual fungal non-CBM carrying GH26 endo-β-mannanase from Yunnania penicillata, Sci. Rep. 9 (2019) 2266, https://doi.org/10.1038/s41598-019-38602-x.
[51] P. von Freiesleben, N. Spodsberg, T.H. Blicher, L. Anderson, H. Jørgensen, H. Stålbrand, A.S. Meyer, K.B.R.M. Krogh, An Aspergillus nidulans GH26 endo-β-mannanase with a novel degradation pattern on highly substituted galactomannans, Enzyme Microb. Technol. 83 (2016) 68–77, https://doi.org/10.1016/j.enzmictec.2015.10.011.
[52] V. Bågenholm, M. Wiemann, S.K. Reddy, A. Bhattacharya, A. Rosengren, D. T. Logan, H. Stålbrand, A surface-exposed GH26 β-mannanase from Bacteroides ovatus: structure, role, and phylogenetic analysis of BoMan26B, J. Biol. Chem. 294 (2019) 9100–9117, https://doi.org/10.1074/jbc.RA118.007171.
[53] X.-X. Yan, X.-M. An, L.-L. Gui, D.-C. Liang, From structure to function: insights into the catalytic substrate specificity and thermostability displayed by Bacillus subtilis mannanase BCman, J. Mol. Biol. 379 (2008) 535–544, https://doi.org/10.1016/j.jmb.2008.03.068.
[54] L. Anderson, P. Hägglund, D. Stoll, L. Lo Leggio, T. Drakenberg, H. Stålbrand, Kinetics and stereochemistry of the *Cellulomonas fimi* β-mannanase studied using ^{1}H-NMR, Biocatal. Biotransformation 26 (2008) 86–95, https://doi.org/10.1080/10242420701788835.
[55] D. Hogg, E.-J. Woo, D.N. Bolam, V.A. McKie, H.J. Gilbert, R.W. Pickersgill, Crystal structure of mannanase 26A from Pseudomonas cellulosa and analysis of residues involved in substrate binding, J. Biol. Chem. 276 (2001) 31186–31192, https://doi.org/10.1074/jbc.M010290200.